THE ASTRONOMICAL JOURNAL, 119:2458–2464, 2000 May

A DIGITAL HIGH-DEFINITION IMAGING SYSTEM FOR SPECTRAL STUDIES OF EXTENDED PLANETARY ATMOSPHERES. I. INITIAL RESULTS IN WHITE LIGHT SHOWING FEATURES ON THE HEMISPHERE OF MERCURY UNIMAGED BY *MARINER 10*

JEFFREY BAUMGARDNER, MICHAEL MENDILLO, AND JODY K. WILSON
Center for Space Physics, Boston University, 725 Commonwealth Avenue, Boston, MA 02215
Received 2000 January 2; accepted 2000 February 4

ABSTRACT

We present an instrumentation plan for spectral imaging of Mercury's extended atmosphere. The approach depends upon simultaneous short-exposure images in white light and sodium, with the former used to select the frames for postintegration of the sodium images. The effects of atmospheric seeing are thus minimized by the combination of high-speed exposures and subsequent selective integration. The instrumentation to be used is a long-slit imaging echelle spectrometer equipped with an image slicer and an imaging photon detector. A test of the white-light component of the technique has yielded a best-to-date image of a portion of Mercury's surface not photographed during the *Mariner 10* mission.

Key words: planets and satellites: general — planets and satellites: individual (Mercury) — solar system: general — techniques: miscellaneous

1. INTRODUCTION

The classic approach to imaging faint structures is to use the best available detector system with the longest exposures allowed by scattered light and atmospheric seeing conditions. If the target observed is stable in space and time, for large telescopes the factor that determines resolution is the degree of wave-front distortion imposed by random atmospheric turbulence during the exposure time. The solution to the "seeing problem" most often used is to employ adaptive optics, i.e., a computer-controlled deformation of the telescope optics to compensate for the effects of turbulence upon the image. A comprehensive treatment of such methods is given by Roggemann & Welsh (1996 and references therein).

Prior to the application of sophisticated technological solutions to atmospheric seeing problems, it was realized by virtually all expert naked-eye observers that instants of clarity occurred when telescopes performed at their theoretical "diffraction limited" abilities. Unfortunately, the detector in use (the human eye) did not have permanent storage capabilities, and so detailed drawings were made that merged the observer's observational skills with artistic abilities, psychological aspects of pattern recognition, and the unconscious desire to see new things. Yet, some of the more remarkable discoveries in astronomy were made precisely in this way, from Christian Huygens's description of the rings of Saturn to the discovery of Jupiter's red spot and the determination of Mars's rotation rate by J. D. Cassini. Less successful, but certainly more dramatic, were the renderings of features on Mars as glimpsed early in the 20th century. The "canals of Mars" described by Percival Lowell (1895, 1906, 1908) in the US, and the larger scale features portrayed by William ("eagle eye") Dawes in the UK, have been treated by many authors (e.g., Hoyt 1976; DeVorkin & Mendillo 1979). Still, the core argument put forward by Lowell, namely, that the human eye can see in a split second what no camera can record, remains a challenge to the present day.

In this paper we outline an approach based upon the modern formulation of Lowell's grand idea, namely, high-speed imaging coupled to a digital image storage system. The basis of the technique is described by Fried (1978) and in the excellent monograph by Roggemann & Welsh (1996). We chose as our test target the planet Mercury because adaptive optics approaches do not lend themselves easily to daytime observing and the *Hubble Space Telescope* is forbidden from observing an object so close to the Sun. In addition, preliminary results reported by Warell, Limaye, & Lagerkvist (1998) show that albedo features on Mercury's regolith can be seen in ground-based broadband imaging.

2. SCIENTIFIC INTEREST IN MERCURY

While spacecraft have visited all of the planets in the solar system except Pluto, Mercury remains a very much undersampled body. The *Mariner* program succeeded in conducting three flybys of the planet in 1974–1975 that, due to the resonances of orbital encounter geometry, viewed the same half of the planet (longitudes 10°–190°). New missions to Mercury are now planned by NASA and ESA. Given the gap of over 25 years in space-based observations, it is not surprising that new and sophisticated ground-based methods are being applied to the study of the Hermean environment. The longest series of these have been radar studies of the planet in which radio echoes are cast into equivalent bright and dark regions based upon their reflective characteristics (e.g., Goldstein 1971; Slade et al. 1999).

An equally remarkable use of ground-based capabilities has been the spectroscopic detection of atmospheric gases (Na and K) by several groups (Potter & Morgan 1985, 1986, 1987, 1990; Killen, Potter, & Morgan 1990; Sprague, Kozlowski, & Hunten 1990; Sprague et al. 1997a). Two-dimensional imaging of the surface's spectral signatures has also been successful at several wavelengths. Ground-based measurements in the infrared (McCord & Clark 1979; Vilas, Leake, & Mendell 1984; Sprague et al. 1997b) have been used to search for the chemical composition of Mercury's surface, and airborne observations (Emery et al. 1998) for its thermal characteristics. Microwave observations (e.g., Mitchell & de Pater 1994) are also used to explore surface composition.

The spectroscopic data sets published to date portray the spatial distribution of sodium just above Mercury's limb. For more extended regions, there is one filtered two-dimensional image published (Potter & Morgan 1997b). The comet-like appearance in that image has a sodium coma over a spatial scale (2–5 Mercury radii) larger than estimated by theory and simulation work (Smyth & Marconi 1995) for a specific range of ejection speeds. In a more recent study, Potter, Killen, & Morgan (1999) did not see such an extensive atmosphere. Thus, there is a real need for new and independent studies of the Hermean atmosphere. Identification of the size and shape of Mercury's transient sodium atmosphere is, in itself, a central goal in studies of the sources and sinks of planetary exospheres (Morgan & Killen 1997; Hunten & Sprague 1997). Moreover, the relevance of such work is fundamental to our understanding of the similarly produced "surface boundary exosphere" of the Moon (Stern 1999).

The linkage between remotely sensed surface characteristics (thermal and compositional), radar returns, and atmospheric signatures at Mercury (Sprague, Schmitt, & Hill 1998) awaits its final synthesis. In this paper, we describe a new approach for much needed data acquisition methods on Mercury's surface and atmosphere. Initial results are promising in that pilot studies in nonspectral mode have led to a new surface map of regions not viewed by the *Mariner 10* spacecraft.

3. INSTRUMENTATION

The application of monochromatic imaging techniques to Mercury presents some problems not encountered while observing other planetary targets. Since Mercury is always observed in twilight or daytime conditions, one needs to use a high ($\sim$1 Å) spectral resolution instrument to discriminate against the background continuum. In addition, Mercury's radial velocity relative to the Sun and Earth varies considerably with viewing geometry, requiring any spectral element to track the Doppler-shifted wavelength of interest, or to have a large free spectral range to include this shift.

An interference filter can be tuned by heating or tilting, but it is difficult to produce filters with a 1 Å bandpass. Fabry-Perot interferometers have been used to observe the planets at high spectral resolution (e.g., Smyth et al. 1995), but unless a twin-etalon system is used, they do not have a large enough free spectral range to accommodate the large (3 Å) shift possible with a target such as Mercury. A high-resolution grating spectrometer has the required spectral range and resolution but suffers from having a narrow slit that can only view a slice of a planet at any given time. To produce an image of an extended object such as a planet, the slit must be scanned across the disk, consequently losing the time multiplex advantage of the filter and the etalon approaches mentioned above.

A new type of long-slit echelle spectrograph has been developed at Boston University to study the terrestrial dayglow and aurora. These instruments, collectively called HiTIES (High-Throughput Imaging Echelle Spectrometer), share some common features: long ($\sim$50 mm) input slits, reasonably fast (f/3.4 or f/10) collimators, and no cross-dispersing elements. The image of the slit fills the spatial dimension of the detector. Interference filters are used to sort the various orders appearing on the detector. The medium-resolution ($R \sim 10{,}000$) variant of HiTIES uses a mosaic of filters near an image plane to select multiple lines of interest (Chakrabarti 1998). The high-resolution ($R \sim 60{,}000$) instrument uses interchangeable filters to select $\sim$40 Å regions around a given line of interest.

To adapt these instruments to planetary monochromatic imaging, a spatial multiplexer or image slicer is used. Image slicers have long been used with slit spectrometers to study the planets, and in particular Mercury by Potter and colleagues (Potter & Morgan 1990, 1997a; Potter et al. 1999). The image slicer we will use is made by bundling 400 individual 125 μm diameter fibers into a square matrix on 145 μm centers at one end, and a line at the other end. The position of the fibers on the square end of the bundle will be held to a tolerance of ± 10 μm of their ideal positions in a square matrix on 145 μm centers. Such bundles are being produced regularly by Fiberguide Industries of Stirling, New Jersey. The line end of the fiber bundle will serve as the input slit to the spectrometer. The net result is that a two-dimensional image of a planet is remapped into a one-dimensional image that can be dispersed, selected in wavelength space, and then reassembled as a monochromatic two-dimensional image.

The square packing of the fibers in the image slicer results in a nominal efficiency of $\sim$40%, but a microlens array will be used to maximize the coupling of the light into the fibers. This array consists of 400 square lenslets (focal length 2.0 mm) arranged in a 20×20 matrix on 145 μm centers. Similar lenslet arrays are being produced by Adaptive Optics Associates, Inc., of Cambridge, Massachusetts. Each lenslet in this array serves as a field lens imaging the pupil of the telescope onto the 100 μm core of the fibers. The addition of this lens improves the fill factor of the image slicer to almost 100% at the expense of decreasing the f-number at the input (and the output) of the fibers. Thus, while the telescope feeding the image slicer will be $\sim$f/20, the f-number of the collimator of the spectrometer will be faster ($\sim$f/8) in order to accept this output beam. The line end of the image slicer will be polished to a concave curve to fit the focal surface of the collimator and fitted with a single double-convex field lens to direct the light from all parts of the slit onto the collimator.

A schematic of the monochromatic imaging system is shown in Figure 1. A preslit (i.e., pre–image slicer) viewer will be used to pick off $\sim$10% of the beam for conventional broadband imaging to aid in pointing and, more importantly, to aid in subsequent selection and proper registration of images for co-adding. A later version of this preslit viewer will use a dichroic beam splitter that will allow $\sim$95% of the out-of-band light to go to the viewer and $\sim$80% of the on-band (half-power full width HPFW $\sim$ 50 Å) light to go to the spectrograph. The procedure will be to record both the broadband image and the spectrograph image simultaneously at 60 images per second using a "real time" digitizer and a 72 Gbyte disk array in a Pentium computer. The two cameras will be identical except that the camera on the spectrograph will be intensified, similar to those described in Baumgardner, Flynn, & Mendillo (1993). The images from the spectrograph, after selecting a bandpass and reassembling a two-dimensional monochromatic image, will not have sufficient signal-to-noise ratio in a single video field to determine quality of the seeing or precisely where the target is in the frame. The data from the broadband camera will be used to determine when the seeing is good and to find the optimum shift values.

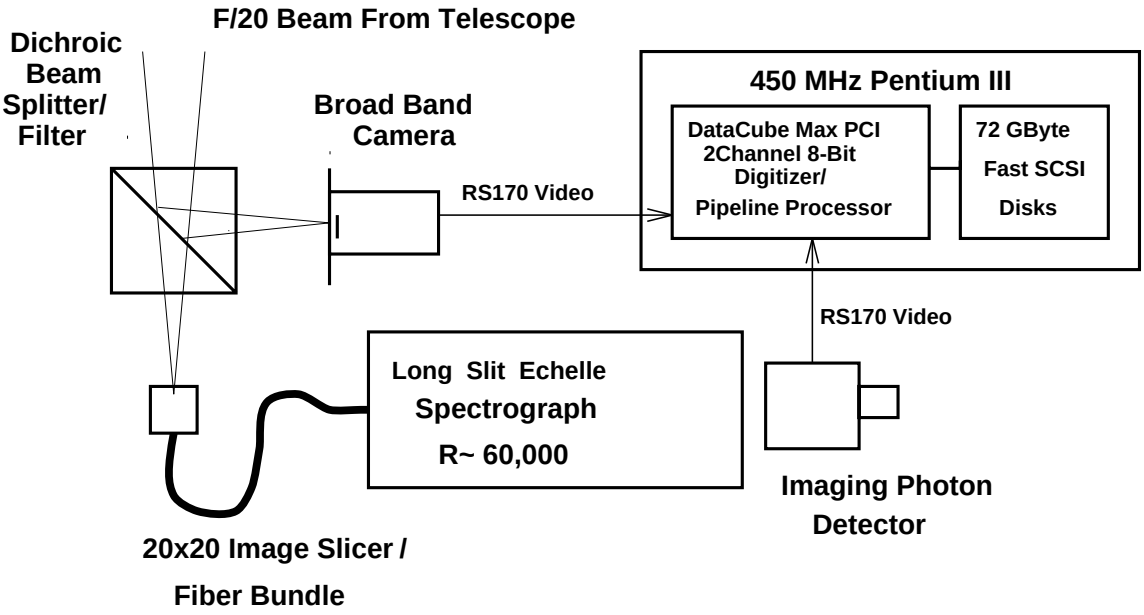

FIG. 1.—Schematic of the high-definition imaging system designed for integrated spectral imaging through a turbulent atmosphere

These values then will be used to align the reconstructed spectrograph images. We believe that this will be the first time this technique of combined beam splitting and shifting and adding is used with an image slicer and a spectrograph to produce nearly diffraction-limited monochromatic images of planets.

4. TEST CAMPAIGN

An opportunity to test some of the components of the system described above occurred in 1998 August. The 60 inch (1.5 m) telescope at Mount Wilson Observatory was used for video imaging of Mercury with an early version of the digital recording system. A commonly available CCD surveillance camera (GBC CCD-505E) was used as a detector. This camera has the highest sensitivity and best signal-to-noise ratio of any RS-170 camera tested. When coupled with the 60 inch f/16 telescope, the plate scale is $\sim 0\farcs09$ pixel^{-1} (at 60 km pixel^{-1}). The diameter of the Airy disk for this aperture at 600 nm is $\sim 0\farcs2$, or 2 pixels.

Since the throughput of the prototype digital imaging system was only 3 Mbyte s^{-1}, it was possible to save only a region of interest (ROI) centered on Mercury. The analog signal from the camera was digitized to 640 × 484 × 8 bits, corresponding to a field of view of $\sim 58''$ horizontally by $\sim 44''$ vertically. Only a 130 × 130 ($12'' \times 12''$) array was written to the computer memory. After approximately 10 s of observations the data were written into a file on the disk. After about 15 minutes of observations, this file on the disk was closed and another file was created. At the end of the observation period for a given day, the data were backed up on CD-ROMs.

During the observations, the 84 pixel diameter image of Mercury was moved around in the video frame to average out pixel-to-pixel variations and to avoid known blemishes on the chip. The 130 × 130 pixel ROI was manually tracked on Mercury as the image moved around on the chip.

Mercury was observed for about an hour on each of 4 days in 1998 August. The observations typically began about one half-hour before sunrise. After sunrise, the dome shutter and windscreen were used to shield the telescope optics and structure from direct sunlight. Once the Sun was at more than $\sim 5^\circ$ elevation, sunlight began heating the telescope structure, causing the focus to change and a noticeable degradation of the seeing. Table 1 lists the circumstances for the observations of Mercury made on 1998 August 27, 28, 29, and 30.

5. DATA REDUCTION

The individual images were saved as "tiles" in large (~650 Mbyte) files. Each file consists of ~100,000 individual, 1/60 s exposures. A series of tests was developed so that

TABLE 1

MERCURY OBSERVATION PARAMETERS FOR 1999 AUGUST

Parameter	Aug 27	Aug 28	Aug 29	Aug 30
Fraction illuminated	0.284	0.323	0.364	0.406
Phase angle (deg)	115.9	110.9	105.9	101.0
Diameter (arcsec)	8.2	7.9	7.7	7.5
Sub-Earth longitude (deg)	242.8	248.4	253.9	259.2
Sub-Earth latitude (deg)	+8.3	+8.0	+7.7	+7.5
Subsolar longitude (deg)	358.7	359.3	359.8	0.2
Number of images	~5,000	~200,000	~300,000	~80,000

the computer could sort these images and reduce the number to a few hundred suitable for co-adding. The data from 1998 August 29 were chosen for further reduction.

After eliminating all fields in which the entire image of Mercury was not visible (e.g., the image was cut off because of tracking errors), the remaining 219,000 images were characterized by a rotation angle (the camera was removed from the telescope several times during the observation period) and average sharpness or contrast. We used an image operator that effectively calculates the pixel-by-pixel contrast in an image:

$$\text{contrast at pixel } (i, j) = |\,\text{pixel } (i, j) - \text{pixel } (i + 1, j + 1)| + |\,\text{pixel } (i + 1, j) - \text{pixel } (i, j + 1)|\,.$$

Images were first smoothed to reduce pixel-to-pixel noise, the contrast operator was then applied, and the resulting images were squared to enhance small regions of high contrast (e.g., the limb) over large regions of low contrast (i.e., shades of gray across the crescent due to illumination). Finally we summed over the entire image to get a single number, or sharpness score, for each image. Figure 2 is a histogram of the sharpness scores for the 219,000 images used from August 29. Figure 2 also shows examples of images with low, medium, and high sharpness scores.

The top 1000 images were reordered by considering their distortion, or "rubber sheeting." Each image was compared with the average shape and then sorted by grouping the most similarly shaped images together. The top 30 images from each rotation were subpixel-shifted by keying on one image in the group, and then co-added. The images were expanded by a factor of 2 in the y-direction to regain the correct aspect ratio before shifting and co-adding. The results of this procedure for the data taken on August 29 are shown in Figures 3*a* and 3*b*. For comparison, Figure 3*c* is the result of co-adding 30 consecutive video fields without shifting or selecting them for sharpness.

The images in Figures 3*a*–3*c* have improved signal-to-noise ratio as compared with the single video fields shown in Figure 2. Figures 3*d*–3*f* are the same images as in Figures 3*a*–3*c* but have been sharpened using a maximum entropy method of deconvolving a point-spread function (PSF) from the images. Since no star was observed simultaneously with Mercury, the limb profile of the co-added images was used to estimate the initial PSF. For these images, a Gaussian profile with an HPFW of 4 pixels was used (yielding an effective resolution of ~250 km). Figures 3*d* and 3*e* show much improved surface detail, whereas Figure 3*f* has a mottled appearance due to the reinforcement of fixed pattern noise on the CCD. (No suitable flat fields were

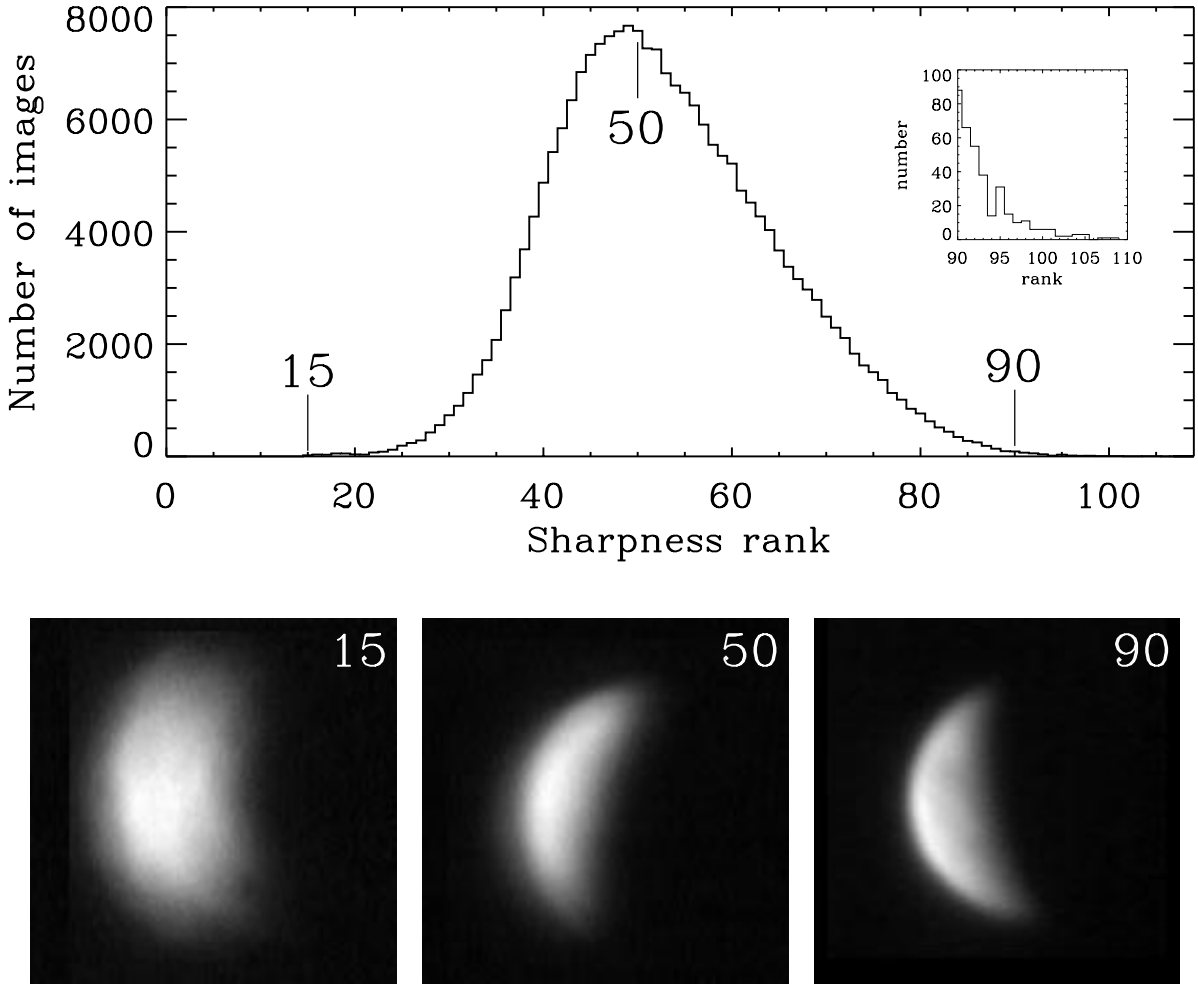

FIG. 2.—*Top*, distribution of approximately 219,000 images taken on 1999 August 29, sorted by their image sharpness as determined by the contrast algorithm rank; *bottom*, sample images illustrating the effectiveness of the contrast-rank method of automated image selection for postintegration.

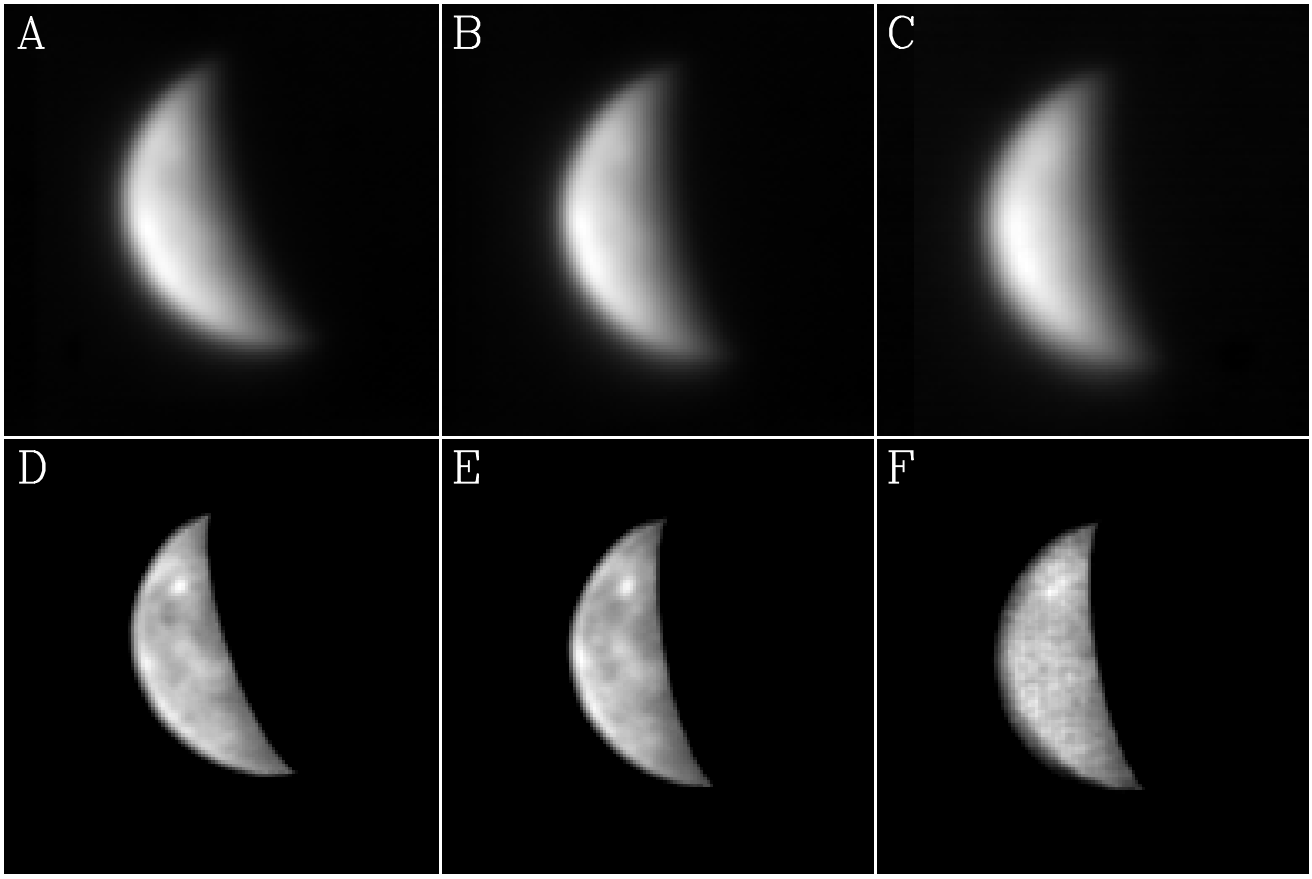

FIG. 3.—Combined and processed images of Mercury from 1999 August 29. In the interest of preserving as much detail as possible, these images have not been rotated from their original orientation on the camera. (*a*, *b*) Averages of the best 30 images for each of two camera rotation angles. (*c*) Average of 30 consecutive "typical" video images without shifting. (*d–f*) Maximum entropy deconvolution of images (*a*), (*b*), and (*c*), respectively. To further enhance surface features, these images were divided by a function equal to the square root of the cosine of the local solar zenith angle.

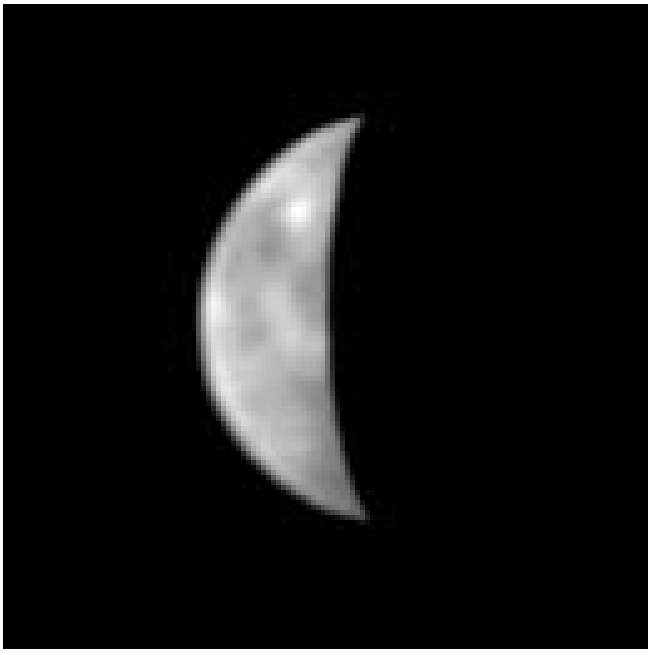

FIG. 4.—Combined average of the 60 best Mercury images of 1999 August 29, from Figs. 3*d* and 3*e*.

available to correct the images before adding.) This fixed pattern noise is randomized in Figures 3*d* and 3*e* because the component images are taken from different regions on the CCD. Figure 4 is the average of Figures 3*d* and 3*e* and represents our overall portrayal of Mercury on this day. The rotation of both panels to portray a vertical terminator reduces pixel-to-pixel variations at the expense of smoothing contrast features seen more clearly in Figures 3*d* and 3*e*.

6. DISCUSSION

The illuminated portion of Mercury shown in Figure 4 was not observed by the *Mariner 10* spacecraft, so no "satellite truth" is available to gauge how well the images match reality. The fact that Figures 3*d* and 3*e* show substantially the same features even though they were made from a different set of images is encouraging. While no *Mariner* images exist for the portion of Mercury shown in Figure 4, there are several ground-based data sets available for comparison. Radar observations cover all longitudes, and several interesting echo features have been identified. Most interest has been given to the polar regions, where radar "bright spots" have been shown to be essentially coincident with large craters imaged by *Mariner 10* (Harmon et al. 1994). The possibility that the source of the enhanced reflectivity is water ice in permanently shadowed

craters is an area of intense study (Moses et al. 1999; Vasavada, Paige, & Wood 1999; Barlow, Allen, & Vilas 1999; Killen, Benkhoff, & Morgan 1997; Sprague, Hunten, & Lodders 1995; Ingersoll, Svitek, & Murray 1992, and references therein). We cannot add to this discussion of polar features with the images obtained in this pilot study, since the view of high latitudes was far from ideal. At midlatitudes, however, radar bright spots have been observed at three specific locations, designated as A (S30°, W350°), B (N55°, W345°), and C (N15°, W240°).

To compare the radar and optical data, we map the image of Mercury from Figure 4 onto a Mercator projection, shown in Figure 5. *Mariner 10* data provided by C. J. Hamilton[1] are also included for reference. The left edge of the mapped region in Figure 5 is the limb, and the right edge marks the terminator.

Harmon (1997) and Harmon & Slade (1995) suggested that radar feature A is a large, relatively fresh impact crater and that B resembles a shield volcano as seen on Venus or Mars. Sprague et al. (1998) reported atmospheric sodium enhancements associated with both A and B. We see in Figure 5 no obvious correspondence between feature B (the only radar bright spot in our imaged longitude sector) and surface albedo patterns. Both A and B, in fact, fall close to high relative brightness patterns, but no convincing correlation exists. Interestingly, virtually all of the craters seen in the *Mariner*-imaged sector have no obvious radar signature (judging by Fig. 6 in Harmon 1997). Yet, the brightest albedo feature we see (~N35°, ~W300°) and the nearby equatorial bright area at ~330° west do fall near moderate radar echo locations. The large dark mare-like region at ~15°–35° north over the 330°–300° west longitude sector falls within the weakest radar echo areas in the northern hemisphere radar map. Finally, in the southern hemisphere we see a relatively featureless region in the full longitude sector imaged, again consistent with the bland radar map for that region (Harmon 1997).

[1] See http://planetscapes.com/solar/eng/mercmap.htm.

7. SUMMARY

A pilot study was conducted to test a new approach to spectral imaging of Mercury's tenuous atmosphere. The goal of simultaneous high-definition imaging in white light and in sodium emission involved an initial campaign to test data acquisition at fast digital rates, as well as automation algorithms for image selection. The data set obtained at the Mount Wilson Observatory on 1998 August 29 included portions of Mercury's surface not photographed during the *Mariner* program. The optical images show Mercury albedo features over the longitude range 270°–360° west. Spatially variable features are seen with a resolution of approximately 250 km. They are more prominently visible in the northern hemisphere, with appearances reminiscent of low-resolution photographs of the Moon. A bright feature in the northern hemisphere appears similar to naked-eye views of the lunar crater Copernicus when seen at last quarter in the morning sky; the darker features are similar in appearance to lunar maria.

Radar maps of Mercury show the planet to be somewhat bland in reflective characteristics except at the poles and at three sites at midlatitudes. One of these radar bright spots (termed "B" in Harmon 1997) is within the longitude sector imaged, but there is no obvious relation to our albedo map, or to the sodium seen near B by Sprague et al. (1998). The relationships between white-light signatures, radar backscatter, and reflectance spectroscopy are far from certain even in the *Mariner*-imaged hemisphere.

Operationally, the digital recording system worked well, but the complete system will have to improve the throughput to disk by at least a factor of 2 since data will be obtained from two cameras simultaneously. Given that the narrow bandwidth (~1 Å) of the monochromatic imager will reduce the signal in the spectral image by 3 orders of magnitude, many more images will have to be co-added to achieve a sodium image approximately equivalent to the white-light shown in Figure 4. To find this many images, the criteria for what constitutes a "good" image may have to be broadened.

The procedures described above will be applied to the

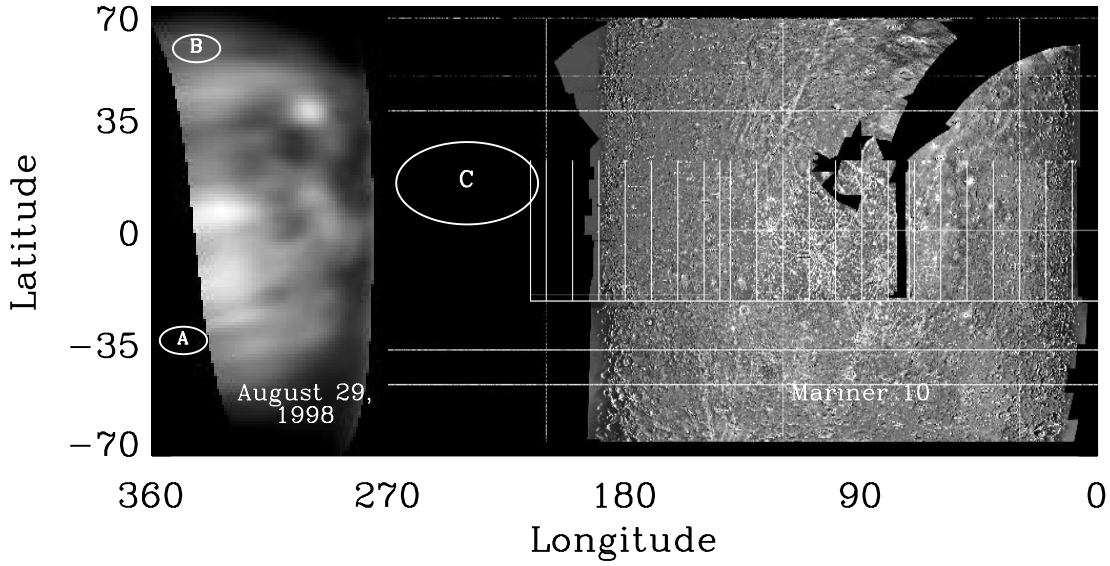

FIG. 5.—Mercator projections of Fig. 4 and of *Mariner 10* data (from C. J. Hamilton). Radar bright spots A, B, and C are shown for comparison.

less favorable data taken on August 27, 28, and 30. Some improvement in the images may be gained by segmenting the images into smaller regions (Dantowitz 1998), recording a separate contrast number for each region, and then reassembling complete images of Mercury.

The data used in this paper were obtained through a cooperative effort between the Center for Space Physics at Boston University and Ron Dantowitz of the Boston Museum of Science and Marek Kozubal. A companion paper appears in this issue describing the reduction of the analog (videotape) data of Mercury taken in 1998 August at Mount Wilson (Dantowitz, Teare, & Kozubal 2000). We are grateful to the Director and staff of the Mount Wilson Observatory for their cooperation during these experiments. This work was supported by seed research funds made available via the Center for Space Physics at Boston University. We acknowledge the assistance of Mead Misic in the data analysis work, Clem Karl and Truong Nguyen for their helpful comments and discussion, and Supriya Chakrabarti for his support of the project. At Datacube, Inc., we acknowledge the assistance of Stan Karandanis and Chuan Zheng. Funding for instrumentation development has been provided by the Office of Naval Research.

REFERENCES

Barlow, N. G., Allen, R. A., & Vilas, F. 1999, Icarus, 141, 194
Baumgardner, J., Flynn, B., & Mendillo, M. 1993, Opt. Eng., 32, 3028
Chakrabarti, S. 1998, J. Atmos. Sol.-terr. Phys., 60, 1403
Dantowitz, R. 1998, S&T, 96(2), 48
Dantowitz, R. F., Teare, S. W., & Kozubal, M. J. 2000, AJ, 119, 2455
DeVorkin, D. H., & Mendillo, M. 1979, Connecticut J. Sci. Educ., 16, 4
Emery, J. P., Sprague, A. L., Witteborn, F. C., Colwell, J. E., Kozlowski, R. W. H., & Wooden, D. H. 1998, Icarus, 136, 104
Fried, D. L. 1978, J. Opt. Soc. Am., 68, 1651
Goldstein, R. M. 1971, AJ, 76, 1152
Harmon, J. K. 1997, Adv. Space Res., 19, 1487
Harmon, J. K., & Slade, M. A. 1995, BAAS, 27, 1116
Harmon, J. K., Slade, M. A., Velez, R. A., Crespo, A., Dryer, M. J., & Johnson, J. M. 1994, Nature, 369, 213
Hoyt, W. G. 1976, Lowell and Mars (Tucson: Univ. Arizona Press)
Hunten, D. M., & Sprague, A. L. 1997, Adv. Space Res., 19, 1551
Ingersoll, A. P., Svitek, T., & Murray, B. C. 1992, Icarus, 100, 40
Killen, R. M., Benkhoff, J., & Morgan, T. H. 1997, Icarus, 125, 195
Killen, R. M., Potter, A. E., & Morgan, T. H. 1990, Icarus, 85, 145
Lowell, P. 1885, Mars (London: Longmans, Green)
———. 1906, Mars and Its Canals (New York: Macmillan)
———. 1908, Mars as the Abode of Life (New York: Macmillan)
McCord, T. B., & Clark, R. N. 1979, J. Geophys. Res., 84, 7664
Mitchell, D. L., & de Pater, I. 1994, Icarus, 110, 2
Morgan, T. H., & Killen, R. M. 1997, Planet. Space Sci., 45, 81
Moses, J. I., Rawlins, K., Zahnle, K., & Dones, L. 1999, Icarus, 137, 197
Potter, A., & Morgan, T. 1985, Science, 229, 651
Potter, A. E., Killen, R. M., & Morgan, T. H. 1999, Planet. Space Sci., 47, 1441
Potter, A. E., & Morgan, T. H. 1986, Icarus, 67, 336
———. 1987, Icarus, 71, 472
———. 1990, Science, 248, 835
———. 1997a, Planet. Space Sci., 45, 95
———. 1997b, Adv. Space Res., 19, 1571
Roggemann, M. C., & Welsh, B. 1996, Imaging through Turbulence (Boca Raton: CRC Press)
Slade, M. A., Harmon, J. K., Perillat, P. J., Jurgens, R. F., & Harcke, L. J. 1999, BAAS, 31, 1132
Smyth, W. H., Combi, M. R., Roesler, F. L., & Scherb, F. 1995, ApJ, 440, 349
Smyth, W. H., & Marconi, M. L. 1995, ApJ, 441, 839
Sprague, A. L., Hunten, D. M., & Lodders, K. 1995, Icarus, 118, 211 (erratum 123, 247 [1996])
Sprague, A. L., Kozlowski, R. W. H., & Hunten, D. M. 1990, Science, 249, 1140
Sprague, A. L., Kozlowski, R. W. H., Hunten, D. M., Schneider, N. M., Domingue, D. L., Wells, W. K., Schmitt, W., & Fink, U. 1997a, Icarus, 129, 506
Sprague, A. L., Nash, D. B., Witteborn, F. C., & Cruikshank, D. P. 1997b, Adv. Space Res., 19, 1507
Sprague, A. L., Schmitt, W. J., & Hill, R. E. 1998, Icarus, 136, 60
Stern, S. A. 1999, Rev. Geophys., 37, 453
Vasavada, A. R., Paige, D. A., & Wood, S. E. 1999, Icarus, 141, 179
Vilas, F., Leake, M. A., & Mendell, W. W. 1984, Icarus, 59, 60
Warell, J., Limaye, S. S., & Lagerkvist, C.-I. 1998, BAAS, 30, 1111